



Performance of $\text{Y}_{0.9}\text{Sr}_{0.1}\text{Cr}_{0.9}\text{Fe}_{0.1}\text{O}_{3-\delta}$ as a sulfur-tolerant anode material for intermediate temperature solid oxide fuel cells

Yun-Fei Bu^a, Qin Zhong^{a,*}, Dan-Dan Xu^a, Xiao-Lu Zhao^a, Wen-Yi Tan^b

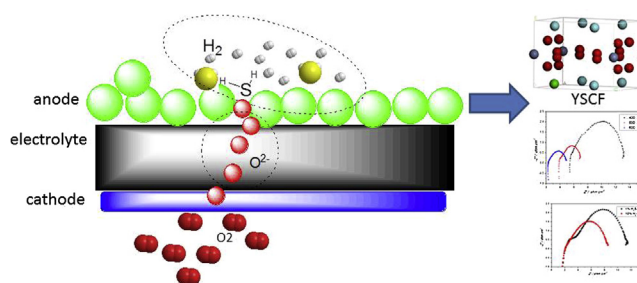
^aSchool of Chemical Engineering, Nanjing University of Science and Technology, Nanjing 210094, China

^bDepartment of Environment Engineering, Nanjing Institute of Technology, Nanjing 211167, Jiangsu, China

HIGHLIGHTS

- $\text{Y}_{0.9}\text{Sr}_{0.1}\text{Cr}_{0.9}\text{Fe}_{0.1}\text{O}_{3-\delta}$ as an anode material for SOFC was examined.
- YSCF was an active anode for the oxidation of the H_2S -containing fuel.
- YSCF was tested by EIS under different gas environment as an SOFC anode.

GRAPHICAL ABSTRACT



ARTICLE INFO

Article history:

Received 20 August 2013

Received in revised form

22 October 2013

Accepted 7 November 2013

Available online 15 November 2013

Keywords:

Perovskite

Solid oxide fuel cell

YSCF anode

Hydrogen sulfide

ABSTRACT

Perovskite-type $\text{Y}_{0.9}\text{Sr}_{0.1}\text{Cr}_{0.9}\text{Fe}_{0.1}\text{O}_{3-\delta}$ maintained good chemical stability under a H_2S -containing atmosphere based on results from X-ray diffraction (XRD) and Fourier transform infrared spectroscopy (FT-IR) in our previous study. In this research, the YSCF-based anode was studied using H_2 and H_2S -containing fuels. The activity of an electrode is closely related to its material composition, lattice structure, physico-chemical properties, and morphologic structure. Therefore, the characteristics of the YSCF powders and the cell were analyzed by XRD, Brunauer–Emmett–Teller (BET) surface area analysis, and scanning electron microscopy (SEM). The conductivities of YSCF were evaluated by four-probe method in 10% $\text{H}_2\text{--N}_2$, 1% $\text{H}_2\text{S--N}_2$ and air, respectively. Thermodynamic calculations and X-ray photoelectron spectroscopy (XPS) analysis have been used to investigate the stability of the elements in YSCF upon exposure to hydrogen sulfide (H_2S) in hydrogen (H_2) over a range of partial pressures of sulfur (p_{S_2}) and oxygen (p_{O_2}) that are representative of fuel cell operating conditions. In addition, the performance of the complete cell (YSCF–SDC|SDC|Ag) under H_2S and H_2 fuel mixtures was also evaluated by electrochemical impedance spectra (EIS) and I – V and I – P curves. The emergence of FeSO_4 in the sulfur treatment should play an important role in preventing further sulfur-poisoning.

© 2013 Elsevier B.V. All rights reserved.

1. Introduction

The disposal and treatment of H_2S is regarded as a worldwide problem. Typically, gas-processing plants convert this toxic gas into

elemental sulfur and water vapor via the well-established Claus process. The reaction is highly exothermic. Part of the energy can be recovered as low-grade energy from the heat and steam produced. Solid oxide fuel cells (SOFCs) are a promising clean power source that is characterized by high energy conversion efficiency, high power density, low environment impact and excellent fuel flexibility [1]. Every oxidation/hydrogenation reaction with negative free enthalpy (equal Gibbs Energy) can be conducted in a fuel cell as membrane reactor with parallel production of electricity. It is

* Corresponding author. Tel./fax: +86 25 84315517.

E-mail addresses: jpu441@yahoo.com (Y.-F. Bu), ZQ304@mail.njust.edu.cn (Q. Zhong).

possible for internal reforming or direct utilization of practical sulfur-containing fuels, which minimizes the need for a separate fuel processor [2]. The feasibility of using H_2S as the fuel for a SOFC simultaneously produces electricity [3], high-temperature steam, and concentrated sulfur dioxide. The SO_2 reaction products may be used in the manufacture of sulfuric acid and sodium hydrosulfite [4]. From economic and environmental perspectives, it is much more desirable to recover this energy as electricity in a highly efficient way.

However, H_2S has a catastrophic effect on typical anode materials for SOFC devices [5]. Sulfur poisoning severely degrades fuel cell stability and electrochemical performance. Effective utilization of sulfur-containing fuels in SOFCs has generated great interest in the development of sulfur-resistant anode materials for SOFCs [6]. Perovskite-type oxides with a general formula of ABO_3 have demonstrated great promise for application in SOFCs [7–10], due to its properties including good redox stability, tunable conductivities, resistance to sulfur poisoning and catalytic activity for fuel under a wide range of operational temperatures. In addition, the perovskite-type structure of oxides expands the possible application, because the original ions at both A- and B-sites can be replaced by other ions that have a similar ionic size and valence, maintaining the original structure. The substitution should enhance the commercial utility of the perovskite device by improving or fine tuning the physical properties such as thermal stability, chemical stability, magnetic effects, catalytic activity and electrolyte compatibility.

As a traditional perovskite-type structure, yttrium chromites (YCrO_3) have been reported with promising utility for the ceramic interconnect material in SOFCs [11–13]. Pure YCrO_3 has the perovskite structure that is apparently stable to at least 1200 K [14]. However, its application is limited due to the relatively low electrical conductivity. An appropriate selection of A and B cations can assist in the generation of materials with good conductivity and stability [15]. By doping with strontium at the A-site, the electronic and ionic conductivity would be enhanced [16,17]. It should be noted that the B-sites are located near the oxide anions. It is often occupied with a transition metal, that possesses suitable redox properties. Doping Fe at the B-site can improve its electrical conductivity under reducing conditions.

In our previous research [11], a series of $\text{Y}_{0.9}\text{Sr}_{0.1}\text{Cr}_{1-x}\text{Fe}_x\text{O}_{3-\delta}$ powders were prepared by the sol–gel combustion method and characterized as potential anode materials for solid oxide fuel cells. By comparing the O1s peaks prior reduction, a lower content of lattice oxygen and a higher content of adsorbed oxygen were observed for $\text{Y}_{0.9}\text{Sr}_{0.1}\text{Cr}_{0.9}\text{Fe}_{0.1}\text{O}_{3-\delta}$ after reduction, which maintained good chemical stability upon exposure to H_2S as determined by XRD and FT-IR analyses. In addition, the reduced $\text{Y}_{0.9}\text{Sr}_{0.1}\text{Cr}_{0.9}\text{Fe}_{0.1}\text{O}_{3-\delta}$ could capture oxygen when exposed to air, which is essential for anode materials. Therefore, in this research, the electrochemical properties of $\text{Y}_{0.9}\text{Sr}_{0.1}\text{Cr}_{0.9}\text{Fe}_{0.1}\text{O}_{3-\delta}$ were measured in a cell with configuration of YSCF–SDC/SDC/Ag at different temperatures even at H_2S higher concentration to examine its sulfur resistance and electrochemical performance.

2. Experimental

2.1. Preparation and characterization

The $\text{Y}_{0.9}\text{Sr}_{0.1}\text{Cr}_{0.9}\text{Fe}_{0.1}\text{O}_{3-\delta}$ anode materials were synthesized by the sol–gel method. The details of the synthesis way have been described in our previously published study [11]. The precursor ash was calcined in air at 1100 °C, 1000 °C, 900 °C, 800 °C or 700 °C for 10 h using a rate of 5 °C min^{-1} . The obtained anode catalyst was denoted YSCF-1100, YSCF-1000, YSCF-900, YSCF-800 or YSCF-700, according to the different calcination temperatures.

For the cell test, the $\text{Ce}_{0.8}\text{Sm}_{0.2}\text{O}_{1.9}$ (SDC) electrolyte was also prepared by the EDTA–citric combustion method [18,19]. After calcination at 900 °C for 6 h under air, the electrolyte was pressed into a pellet with a thickness of 0.8 mm and a diameter of 30 mm. The pellet was sintered at 1450 °C for 8 h to achieve densification.

Specific surface areas of the different catalysts were determined by the BET method. The surface area of the catalyst was determined by N_2 adsorption-desorption measurements at –196 °C using the Brunauer–Emmett–Teller (BET) method (Gold App V-sorb 2008p).

The crystal structure of the YSCF powders before and after the test was determined by X-ray diffraction (XRD; Bruker D8 ADVANCE, Germany) using Cu K α radiation ($\lambda = 0.15406$ nm) at room temperature with a 2θ ranging from 10° to 80°.

The calculations were performed using HSC Chemistry 5.0 [20] to generate phase diagrams of the ternary component systems of Y–O–S, Sr–O–S, Cr–O–S and Fe–O–S. A temperature of the 873 K was chosen on phase diagrams to explore the impact of the operation temperature on sulfur interaction.

To test the sulfur tolerance ability of YSCF, these materials were reduced in a tube furnace at 600 °C for 2 h under 10% H_2 –1000 ppm H_2S and 1% H_2O (all balanced by N_2) with a flow rate of 60 mL min^{-1} . The samples were cooled to room temperature under the same atmosphere. These samples were also examined with X-ray diffraction to determine the phase composition. The surface composition and valence of each element were identified for fresh and reduced powders by X-ray photoelectron spectroscopy (XPS, Thermo ESCALAB 250, US). A monochromatic Al K α source ($h\nu = 1486.6$ eV) was used at a power of 150 W, with a base pressure of 10^{-9} mbar in the analytical chamber. The binding energies were calibrated with respect to the binding energy of C1s located at 284.8 eV. The resolution of all of the spectra was performed with the XPS Peak Program (Version 4.1), by considering the oxygen peaks and related metal ion peaks. The fitted variables included the peak position and peak shape (given some Gaussian/Lorentz product function). The content of different species was calculated based on the integration of the peak areas with background correction in the XPS Peaks Program.

2.2. Cell measurement

To order to increase the thermal compatibility and reduce the interface resistance between the anode and electrolyte, YSCF–SDC (weight ratio of 5:1) was dispersed in a solution containing glycerol, ethylene glycol and isopropyl alcohol [21] (glycerol:ethylene glycol:isopropyl alcohol = 1:15:10) by the ball milling at 45 Hz for 24 h. The mixture was painted on one side of the SDC disks. The membrane electrode assemblies (MEAs) (cell with configuration: anode/electrolyte/cathode: YSCF–SDC/SDC/Ag) were calcined at 900 °C for 2 h. Au mesh was used as a current collector to adhere to on the surfaces of YSCF with Au paste. The anode chamber of the MEAs was under 1% H_2S , 10% H_2 –1000 ppm H_2S and 1% H_2O (all balanced by N_2) or 10% H_2 – N_2 with a flow rate of 60 mL min^{-1} , and the cathode was exposed to the air. The fuel cell tests were performed in a furnace with a coaxial two-tube (inlet and outlet) set-up at each face of the cell sealed by ceramic sealant.

The cell morphology of $\text{Y}_{0.9}\text{Sr}_{0.1}\text{Cr}_{1-x}\text{Fe}_x\text{O}_{3-\delta}$ before and after the tests in H_2/N_2 and H_2S were observed by using scanning electron microscopy (SEM, HITACH S4800, Japan).

The electrochemical effect, such as the anode polarization resistance (R_p) and Ohm resistance (R_o) were measured by recording the electrochemical impedance spectrum measurement using an electrochemical work station (ParSTAT4000). The electrical conductivities by four-terminal DC technique using Ag paste electrodes. The current and voltage were measured using a Keithley2420 source meter at intervals of 5 °C. Over a temperature range

of testing range 300–900 °C with 50 °C as point distance in different atmosphere.

3. Result and discussion

3.1. Structure properties

The BET surface areas of the YSCF-700, YSCF-800, YSCF-900, YSCF-1000 and YSCF-1100 catalysts are 12.6, 10.3, 7.2, 5.9, and 3.7 m² g^{−1}, respectively. The XRD patterns of the YSCF calcined at different temperatures are shown in Fig. 1. The powders are well crystallized compared with the standard card of YCrO₃ (PDF card no. 34-0365). Some impurity peaks were observed in the sample at 800 °C and 900 °C, which is similar to that of the Y₂O₃ parent (JCPDS card No. 47-1274). This result is also in agreement with the result from thermodynamic calculations below. It has been known that the electrical properties of conducting oxide are highly sensitive to its elemental composition, structure and phase purity [22]. A small deviation from the elemental composition or the introduction of a minor amount of impurity phases may result in a significant deterioration in the electronic or ionic conductivity of the oxide [23]. These results indicate that the Y₂O₃ phase might have formed the perovskite-type phases at 1000 °C, which resulted in the decrease of the BET surface area of the YSCF-1000, in addition, a high calcination temperature is favorable for the formation of a perovskite phase. Therefore, 1000 °C was chosen as the calcination temperature. The details of the bulk structure and the thermal stability in a reducing atmosphere (H₂–H₂S) has been studied in our previous research [11].

The reaction of YSCF and SDC with each other is undesirable for the long-term stability of SOFCs. Therefore, the reactivity of YSCF with SDC was further studied. A comparing of the XRD patterns for YSCF, SDC and the mixture of YSCF + SDC (50%: 50% in weight ratio ball milling 24 h) after calcination under air at 1000, 1100, 1200, 1300, 1400 and 1500 °C for 10 h is shown in Fig. 2a and b. The peak indicated by the arrow begins to merge and gradually shift as the temperature increases, which indicates a solid state reaction between the electrolyte and anode has occurred. It is evident that YSCF exhibits good chemical compatibility with the SDC electrolyte at less than or equal to 1000 °C, and no other new phases were detected indicating that no reaction and inter-diffusion of elements occurred within the composite anode below this temperature [24–26].

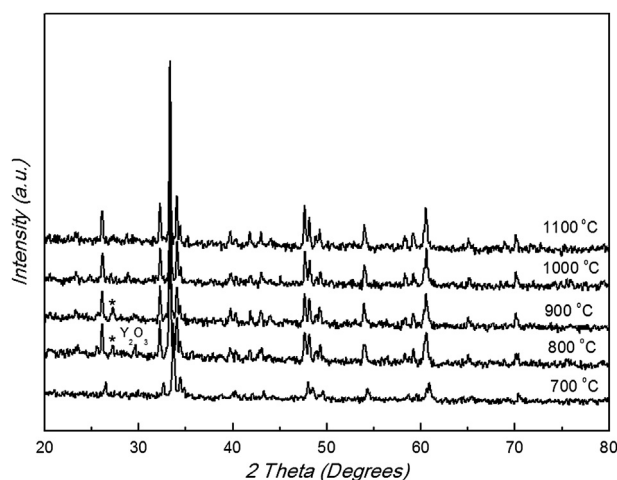


Fig. 1. XRD patterns of Y_{0.9}Sr_{0.1}Cr_{0.9}Fe_{0.1}O_{3-δ} powders calcined at different temperature.

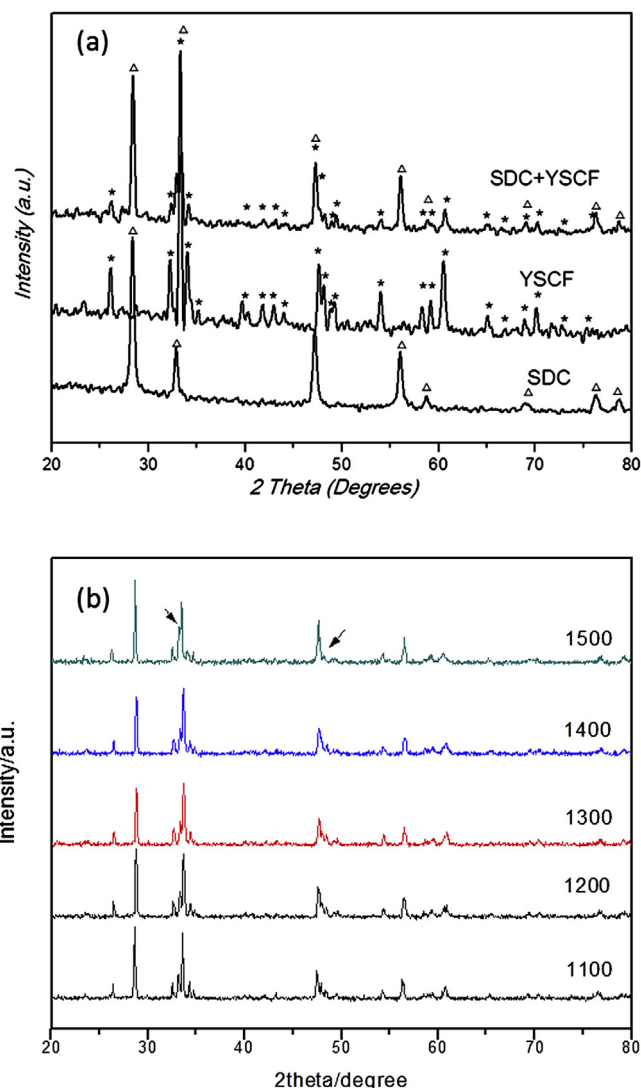


Fig. 2. (a) XRD patterns of YSCF + SDC after calcined in air at 1000 °C for 4 h; (b) XRD patterns of YSCF + SDC calcined in different temperature in air.

3.2. Conductivity testing

The conductivity of YSCF was investigated in air, 10% H₂–N₂ and 1% H₂S–N₂. For perovskite-related MIECs, the co-existence of electronic holes and oxygen vacancies allows them to simultaneously possess both ionic and electronic conductivities. The temperature dependence of the total electrical conductivities of the YSCF samples in different atmosphere is shown in Fig. 3. Sr and Fe co-doping significantly enhances the electrical conductivity of YCrO₃. Fig. 3 shows the temperature dependence of the electrical conductivity of YSCF from 300 to 900 °C. The conductivity increases as the temperature increase, which is a typical characteristic behavior of semiconductors and ionic conductors. Due to an increase in the carrier (i.e. electron–hole) migration rate with the temperature. The nearly linear relationship between ln(σT) and 1/T indicates that the conductivity behavior is a thermally active process associated with the temperature-independent carrier concentration that obeys the small polaron conductivity mechanism expressed in the Eq. (1):

$$\sigma = (A/T)\exp(-E_a/KT) \quad (1)$$

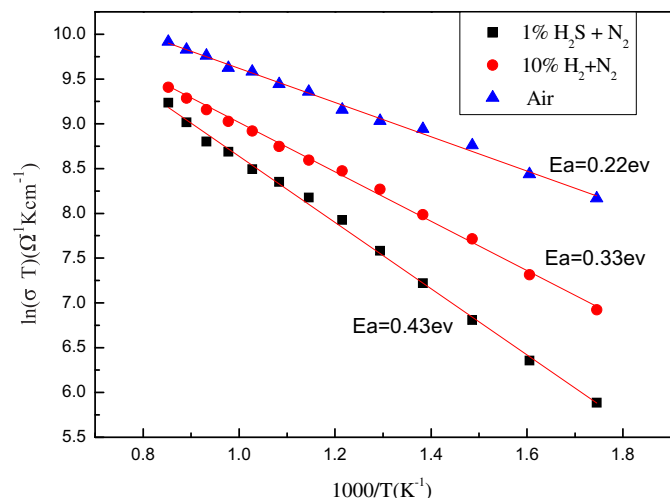


Fig. 3. Plot of $\ln(\sigma T)$ versus $1000/T$ for YSCF under various mix gas in the 300–900 °C temperature interval.

where A is the pre-exponential factor, K is Boltzmann's constant, T is the absolute temperature and E_a is the activation energy. The conductivity in air is higher than that under reduction conditions, because the oxygen loss reduces the carrier concentration resulting in a decrease in the conductivity of YSCF. For the perovskite, the valence state of Y^{3+} and Sr^{2+} remain the same. Doping with smaller valence cation typically forms oxygen vacancies to retain electrochemical neutrality, and the oxide ion conductivity increase as the oxygen vacancies increase. In general, it is believed that doping with transition metal cations, such as Ni or Fe, enhance the electron or hole conduction. The reduction processes (Cr^{6+} , Cr^{4+} to Cr^{3+}) observed upon exposure to H_2 or H_2S at high temperature result in a decrease of conductivity, except for the Fe^{3+} to Fe^{2+} or Fe^0 .

The electrical conductivity in $YCrO_3$ is essentially due to the 3d band in the Cr ions. It is believed that the electronic conduction in the perovskite oxide is achieved via a small polaron hopping mechanism. B-site lattice cations are responsible for the creation of electron defects in perovskite oxides due to strong overlapping of the B–O–B bonds, and the electronic conduction occurs via a mechanism that is similar to a Zerner double exchange. Co-doping will increase the oxygen vacancy concentration but decrease the Cr^{4+} concentration. The former leads to an increase of ionic

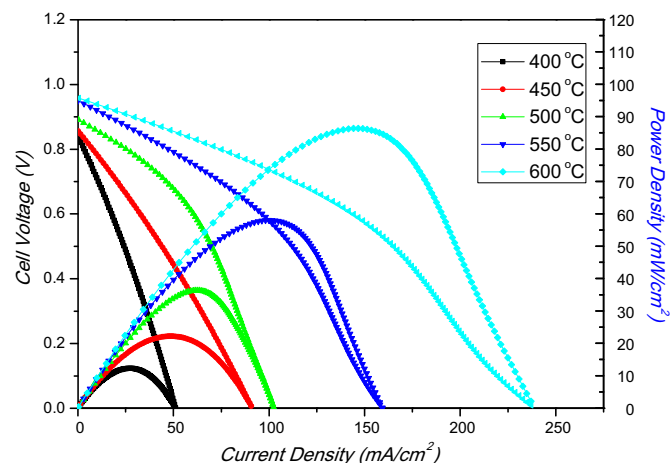


Fig. 4. IV–IP curves of single cell with YSCF anode under 10% H_2 –1000 ppm H_2S fuel at different temperatures.

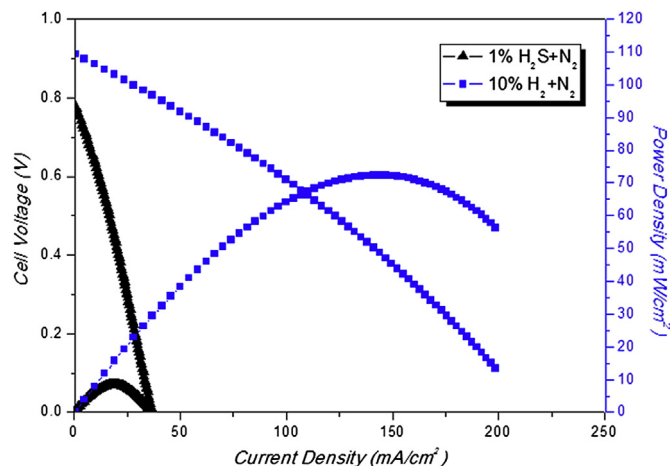


Fig. 5. IV–IP curves of single cell with YSCF anode under 1% H_2S – N_2 or 10% H_2 – N_2 at 600 °C.

conductivity, and the latter results in a decrease in the electronic conductivity. To compare pure $YCrO_3$ [27] to YSCF, the Sr and Fe doping of $YCrO_3$ significantly promoted the conductivity and reduced the activation energy. The anode conductivity will be significantly enhanced under fuel cell operation conditions. Because large amounts of oxygen will be pumped from the cathode through the electrolyte layer to the anode, the oxygen partial pressure will increase.

3.3. Electrochemical performances

Fuel cell tests are conducted to determine the electrochemical activity of the anode material for fuel conversion. Fig. 4 shows the I – V and I – P characteristics of the YSCF–SDC/SDC/Ag under 10% H_2 –1000 ppm H_2S and 1% H_2O (all balanced by N_2). The peak power densities are 12.24, 22.16, 36.23, 58.02 and 86.34 $mW\ cm^{-2}$ at 400, 450, 500, 550 and 600 °C, respectively. The OCV values are 0.84, 0.86, 0.89, 0.95 and 0.96 V at 400, 450, 500, 550 and 600 °C, respectively. The OCV value calculated by the Nernst equation and increase as the temperature increases but to a lesser extent than observed in previous studies. [28] SDC is a promising electrolyte at

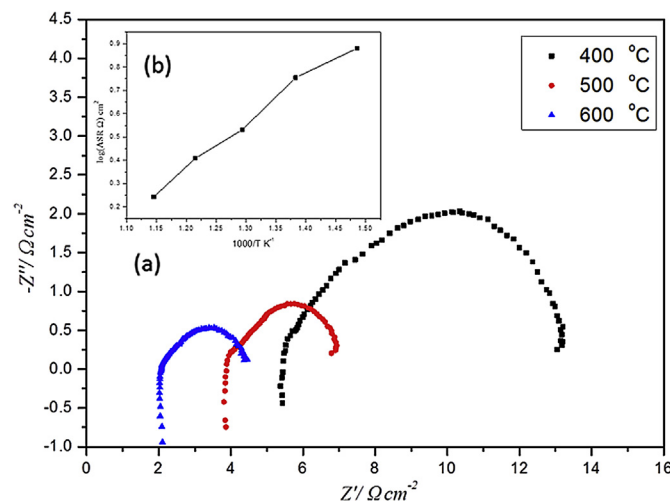


Fig. 6. (a) The impedance spectroscopy of YSCF anode under 10% H_2 –1000 ppm H_2S fuel at 400 °C, 500 °C and 600 °C; (b) Arrhenius plots of the ASR values from 400 to 600 °C.

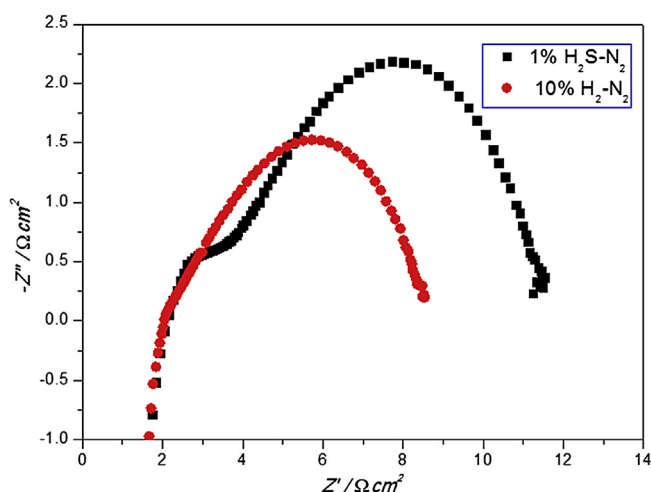


Fig. 7. The impedance spectroscopy of YSCF anode under 10% $\text{H}_2\text{-N}_2$ and 1% $\text{H}_2\text{S-N}_2$ fuel at 600 °C.

intermediate temperatures, because the transport number of the oxide ion increases as the operating temperature increases. However, even a small electron conduction and oxygen leakage through the electrolyte can drastically decrease the energy conversion efficiency [29]. In addition, the linear behavior of $I\text{-}P$ and $I\text{-}V$ is most likely due to the thickness of electrolyte (SDC) which hinders the activation of the YSCF–SDC electrode and the oxygen permeation in the form of O^{2-} . Fig. 5 displays the cell voltage and power density as a function of current density for a typical SOFC single cell. First, the cell is stabilized in 10% $\text{H}_2\text{-N}_2$ fuel with a flow rate of 60 mL min^{-1} at 600 °C. The maximum power density measured for the cell was 72.35 mW cm^{-2} higher than that previously reported for other anode materials under an intermediate temperature. [30]

The OCV reaches 0.91 V, which is nearly 1 V and lower than that of the cell under 10% $\text{H}_2\text{-}1000\text{ ppm H}_2\text{S}$ (balanced by N_2). In addition, the power density at 600 °C in 1% $\text{H}_2\text{S-N}_2$ is 8.31 mW cm^{-2} , and the OCV is 0.78 V. The power density decreases as the concentration of the fuel decreases. The electrochemical performance of the cell under 10% $\text{H}_2\text{-N}_2$ and 1% H_2O is slightly lower than that for the cell under 10% $\text{H}_2\text{-}1000\text{ ppm H}_2\text{S-N}_2$ and 1% H_2O . The reason for this behavior is not very clear because it is contrary to the expected poisoning effect of sulfur on catalysts. One hypothesis for the observed sulfur-enhancement behavior is that the YSCF anode also possesses good activity for the electrochemical oxidation of H_2S . Another possibility is that the surface of the YSCF anode material transformed to a particular surface sulfide when a high concentration of H_2S was present, and this surface sulfide is a better catalyst for the electrochemical oxidation of H_2S . [9,10,29–32] The result is consistent with those obtained from the impedance spectra. Therefore, that the YSCF–SDC exhibits some catalytic activity for the conversion of H_2 , H_2S or a mixture of them in a SOFC [30].

Impedance spectroscopy is used to determine the effect of the operating temperature and H_2S concentration of the fuel cell on the interfacial resistance for cells using YSCF–SDC as an anode. Fig. 6 shows a comparison of the impedance spectra of the whole cell under exposure to 10% H_2 and 1000 ppm H_2S balanced by N_2 at 400–600 °C. The impedance spectra are composed of two selections (i.e., the ohmic resistance (R_{ohm}), and the activation resistance (a sum of the anode and cathode)). In fact, R_{ohm} is the overall ohmic resistances including the electrolyte resistance, the electrode ohmic resistance, the electrode-current collector contacting resistance and the lead resistance. Therefore, the R_{ohm} measurement does not simply reflect the electrolyte resistance. According to Fig. 6, the main loss of the fuel cell was due to the electrode polarization. Figs. 6 and 7 appear to support the results from the cell performance. Because the analysis of the impedance spectra of the fuel cells is complicated, the low frequency area is associated with

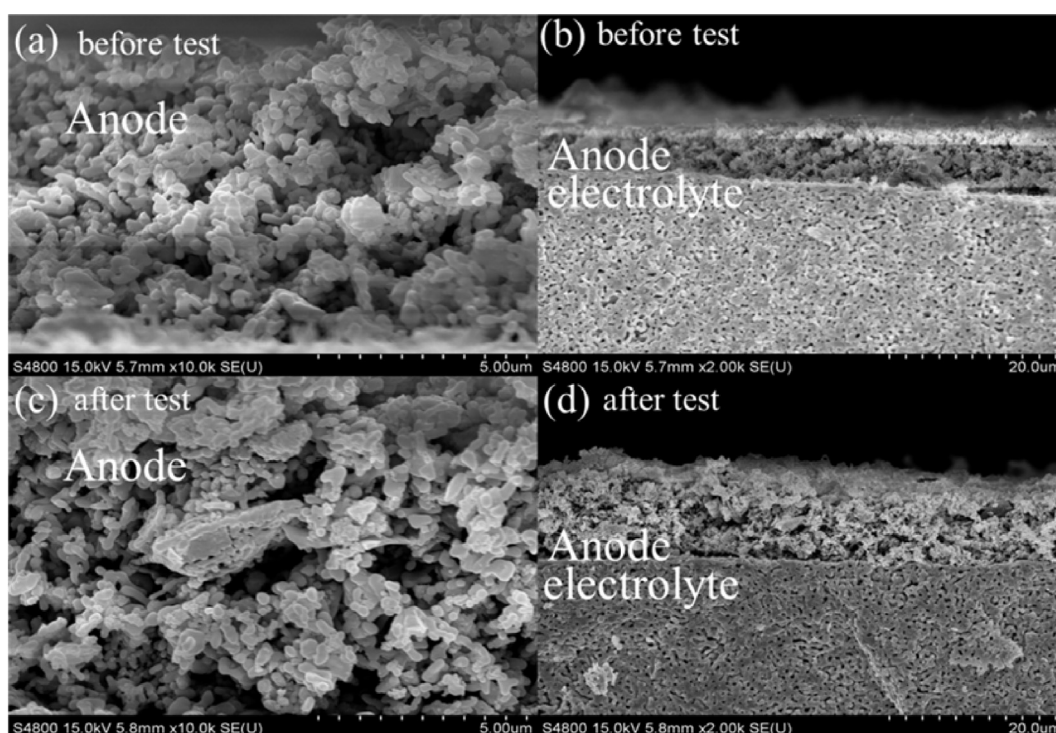


Fig. 8. The SEM pictures of surfaces and cross-sections of the YSCF electrodes before and after cell tests.

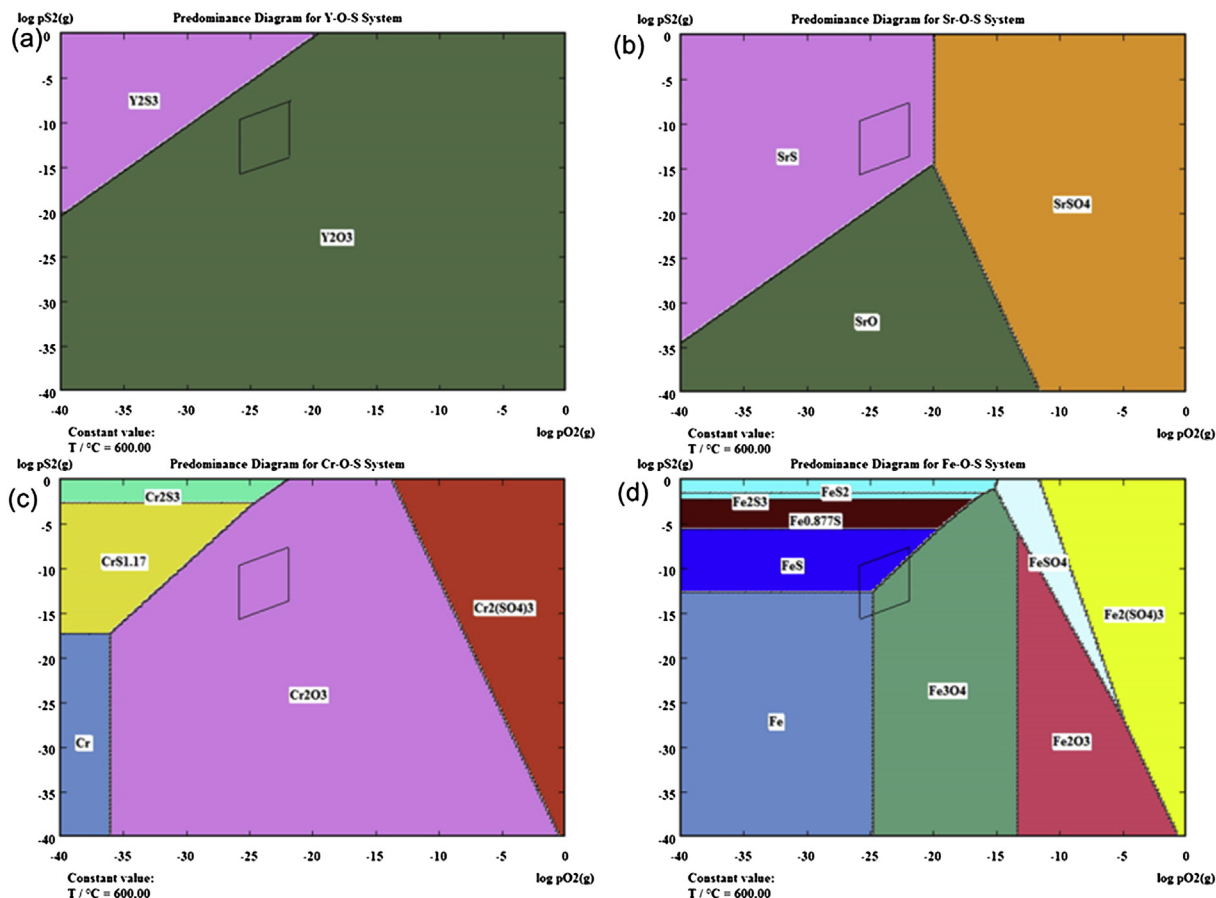


Fig. 9. (a) The phase equilibrium of the Y–O–S system at 873 K. The shaded area shows the phase the phases of Y over an H_2S range of 1–1000 ppm in humidified hydrogen (10% H_2 , 1% H_2O ; i.e. 90% fuel utilization). (b) The phase equilibrium of the Sr–O–S system at 873 K. The shaded area shows the phase the phases of Sr over an H_2S range of 1–1000 ppm in humidified hydrogen (10% H_2 , 1% H_2O ; i.e. 90% fuel utilization). (c) The phase equilibrium of the Cr–O–S system at 873 K. The shaded area shows the phase the phases of Cr over an H_2S range of 1–1000 ppm in humidified hydrogen (10% H_2 , 1% H_2O ; i.e. 90% fuel utilization). (d) The phase equilibrium of the Fe–O–S system at 873 K. The shaded area shows the phase the phases of Fe over an H_2S range of 1–1000 ppm in humidified hydrogen (10% H_2 , 1% H_2O ; i.e. 90% fuel utilization).

gas diffusion and conversion processes [33–37], and the high area is related to the charge transfer process of the electrodes. The polarization resistance of the anode is clearly different for 10% H_2 – N_2 , 10% H_2 –1000 ppm H_2S – N_2 and 1% H_2S – N_2 . The interfacial resistances increased in the presence of the H_2S containing fuel.

3.4. Chemical stability of the catalysts under the reaction environment

The SEM images of the cross-sections and surfaces of the YSCF–SDC composite electrodes are shown in Fig. 8. Fig. 8a and b shows the SEM images of the surfaces and cross-sections of the YSCF–SDC composite electrodes prior to the cell tests. The electrode particles strongly adhere to the electrolyte surface. Therefore, to obtain particles with a fine microstructure, strong adhesion to the electrolyte is required. Fig. 8c and d shows the SEM images of the surfaces and cross-sections of the YSCF electrodes after the cell

tests. The SEM images indicated that the YSCF electrode retained its fine and porous microstructure after cell tests. There was a subtle change in the surface morphology observed between the fresh and reduced cells. This result indicates that reduction does not influence the microscopic features of $Y_{0.9}Sr_{0.1}Cr_{0.9}Fe_{0.1}O_{3-\delta}$. The reduction resulted in a good connection between the YSCF and SDC particles in the YSCF + SDC composite anode and helped to reduce the interfacial resistance. In addition, the SDC enlarged the effective anode surface area due to the higher surface area of the SDC compared to YSCF.

The formation of sulfur compounds on the metallic and ceramic components of the cermet can lead to the loss of active sites at the triple phase boundary (TPB) and the modification of surface properties, which poisons the anode. [38] The limits for practical SOFC operation with respect to pS_2 and pO_2 at the anode should be defined. The boundary values of pH_2 and pH_2O were calculated by assuming a mixture of 1% H_2O and 10% H_2 as the input to the anode,

Table 1
The values of pO_2 and pS_2 for different operating conditions in a range of H_2S from 1 to 1000 ppm (a fuel mixture of 10% H_2 and 1% H_2O was used as the input, with 90% fuel consumption-providing 1% H_2 and 10% H_2O as the output).

Temperature (K)	Input (10% H_2 , 1% H_2O)			Output (1% H_2 , 10% H_2O)		
	pO_2	pS_2 , 1 ppm	pS_2 , 1000 ppm	pO_2	pS_2 , 1 ppm	pS_2 , 1000 ppm
873	1.160×10^{-25}	2.192×10^{-16}	2.192×10^{-10}	1.856×10^{-22}	2.192×10^{-14}	2.192×10^{-8}

representing 90% fuel consumption of a hydrogen fueled SOFC. The limits of pS_2 were defined to represent a H_2S concentration ranging from 1 ppm to 1000 ppm. The pO_2 value was derived from Eq. (2)



The pS_2 was calculated using the correlation between the partial pressure and the equilibrium constant of the two reaction:



and



The values of pO_2 and pS_2 under the same operating conditions were, used to define the area of interest in Fig 9. The values of pO_2 and pS_2 at the limits of different fuel mixture inputs are shown in Table 1. Sr and Fe are not stable when exposed to 1000 ppm of H_2S at 873 K, which suggests that sulfur at this level will affect the bulk properties of the YSCF anode. In addition, the reaction of sulfur on the surface needs to be considered, which would affect the catalytic properties of YSCF. Therefore, XPS was used to investigate the surface.

XPS was employed to analyzed the surface of synthesized sample (YSCF) before and after the H_2S-H_2 (10% H_2 –1000 ppm H_2S-N_2 and 1% H_2O) test. For quantification of the elemental composition and identification of the oxidation states of Y, Sr, Fe, Cr and O, $Y3d_{5/2}$, $Sr3d_{5/2}$, $Fe2p_{3/2}$, $Cr2p_{3/2}$ and $O1s$ were used. In all of the samples, the position of the $Y3d_{5/2}$ is located at 156.4 eV indicating that the oxidation state of Y is +3 which is in good agreement with the reported values [39]. The introduction of Sr^{2+} as a lower valence ion to the A-site in the perovskite structure can produce oxygen vacancies [40]. The results from thermodynamic calculations indicate that SrS and FeS would appear under the considered reaction environment, and the $S2p$ peaks in Fig. 9. The position of the $Y3d$ and $Sr3d$ core level peaks shift to high B.E. These observations are contrary to the generation of SrS under the reaction conditions. Which suggests that S would exist in a high valence state instead of S^{2-} after the reduction. Because there was no obvious displacement of other elements, the XPS spectra covering the spectral regions of $Fe2p$, $Cr2p$, $O1s$ and $S2p$ were evaluated. Cr and Fe have multiple oxidation states including Cr (III), Cr (VI), Fe (II), Fe (III) and Fe (IV). The Fe peaks were assigned to oxidized Fe species, more likely Fe^{3+} type species [41,42]. The binding energies centered at approximately about 710.4 and 711.9 eV may be correspond to the Fe^{3+} cations in the spinel structure, and the binding energy centered at approximately 719.0 eV were attributed to Fe^{3+} , which is the fingerprint of the Fe^{3+} species [42]. After the reaction the binding energies centered at approximately 710.7 and 713.6 eV. The position of $Fe2p_{3/2}$ in the tested powders is in good agreement with the reported values for Fe^{3+} and Fe^{2+} (FeS or $FeSO_4$). For Cr there are two peaks with one peak at 575.3–576.4 eV corresponding to Cr^{3+} and the other one at 579.8 eV corresponding to Cr^{6+} . The oxidation states and relative percentage of the elements in YSCF after the test were determined by XPS. Fig. 10 shows the result of peak fittings for the $Fe2p$, $Cr2p$ and $O1s$ peaks. Table 2 lists the BEs of these peaks as well as the calculated relative percentages. The spectra of $Cr2p_{3/2}$ in the tested powders are decomposed into two components corresponding to the Cr^{3+} and Cr^{6+} species. The peaking fitting results indicate that like fresh powders, the Cr in all of the tested powders exhibit multiple oxidation states similar to the fresh powders, which suggests that the Fe doping produced some disproportionation in the oxidation state of Cr. A comparison of Cr^{3+}/Cr^{6+} before and after the test indicates the conversion of

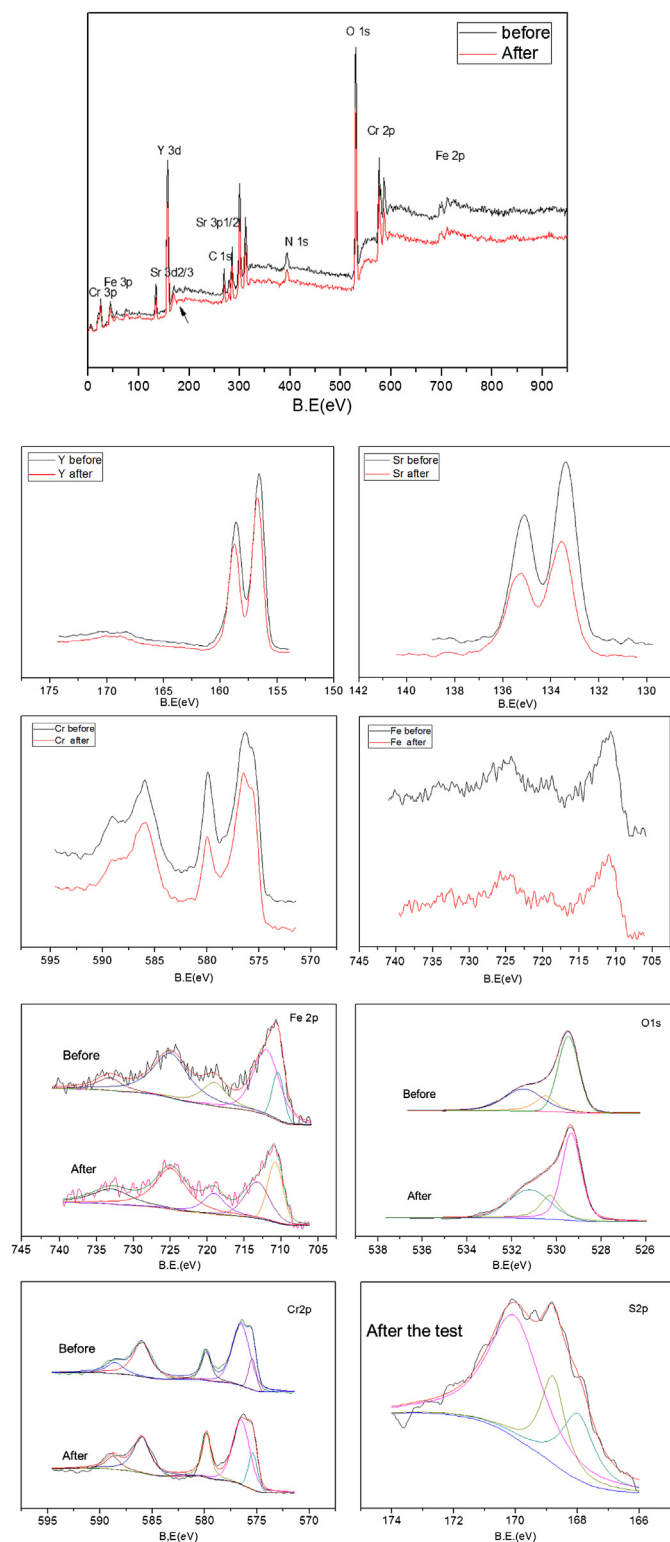


Fig. 10. XPS spectra of YSCF powders as processed before and after the test in 10% H_2 + 1000 ppm H_2S/N_2 .

Table 2
XPS results for the YSCF.

Samples	Fe2p3/2				Cr2p3/2				O 1s			
	Fe3+ Position (eV)	%	Fe2+ Position (eV)	%	Cr3+ Position (eV)	%	Cr6+ Position (eV)	%	Lattice oxygen Position (eV)	%	Adsorbed oxygen Position (eV)	%
Before	710.4 711.9	100%			575.4 576.5	73.92	579.8	26.08	529.3	52.6	530.3 531.2	47.4
After	710.7	47.29	713.2	52.71	575.4 576.5	79.74	579.8	20.26	529.4	52.2	530.5 531.4	47.8

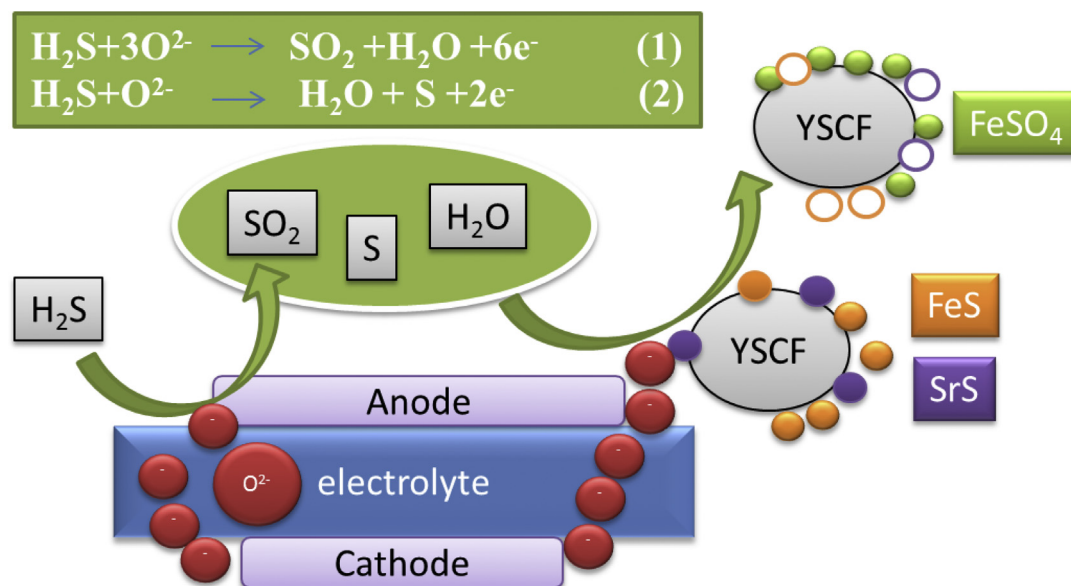


Fig. 11. The schematic drawing of sulfur tolerance of YSCF catalyst.

Cr^{6+} to Cr^{3+} during the reduction process. The S_{2p} peaks at lower binding energies are assigned to S^{2+} , S^{4+} , S^0 and S^{2-} . After the reaction, the sulfur content is low based on the full spectrum, due to many possibilities, such as surface adsorption of the catalyst and so on. Therefore, the analysis should be combined with the condition of sulfur. The XPS sulfur 2p binding energy provides a sensitive measure for the electronic character of sulfur within a molecule. The three peaks located at 167.9, 169.7 and 170.0 eV are assigned to S^{6+} , which confirms the generation of the sulfate mineral (SO_4^{2-}). Oxygen which is bound to metals, especially in metal oxide catalysts, plays an important role in their catalytic properties. The O_{1s} spectrum is frequently used to identify the types of oxygen species presented in a particular oxide. The O_{1s} core level consists of two components, as observed for YSCF. The low B.E. component has been assigned to the lattice oxygen and the high B.E. component corresponds to surface adsorbed oxygen. The relative percentage of lattice and adsorbed oxygen, which is listed in Table 2, is determined from the integrated area of these peaks. The first peak (observed at 529.3–529.4 eV), was attributed to the oxygen ions in the crystal lattice (O^{2-}); The second peak (observed at 530.3–531.4 eV) was assigned to surface adsorbed oxygen species (O^{2-} or O^-), OH groups and oxygen vacancies [43]. These results suggest that the substitution of YCrO_3 generates oxygen vacancies inside the perovskite framework due to the dopants. Due to the presence of oxygen vacancies, it is assumed that lattice oxygen from the bulk would travel through the channels to supply the residual lattice oxygen on the surface, and therefore, a certain amount of lattice oxygen in the bulk of anode catalysts would migrate to the surface. This result suggests that the tested YSCF could maintain its stability

upon exposure to fuel, which is essential for anode materials. There is a stronger interaction between O^{2-} species and B-site metal ions, which results in a slightly higher O_{1s} BE value compared to previously reported values [44]. The presence of Fe and Cr could promote charge transfer from the O atom to other surrounding atoms, shifting the O^{2-} peak towards a higher value. Based on the relative percentage of O species, the content of lattice oxygen is higher than that of surface oxygen species, which means that the former possesses a high catalytic activity. It is well known that the electrical performance is highly sensitive to the elemental composition, structure and phase purity. H_2S may have to react with the residual lattice oxygen before the lattice oxygen migrates to the surface. A schematic representation of the sulfur tolerance of the YSCF catalyst is shown in Fig. 11. Selective oxidation of H_2S may occur under the conditions of limited lattice oxygen, which results in the production of other sulfur species besides sulfate and these various sulfur species coexist on the surface of the sample with H_2 . Therefore, competitive reactions between the addition and consumption of lattice oxygen may participate in the deactivation. These reactions may explain the reason for lower battery performance of hydrogen sulfide lower than hydrogen and the increasing polarization resistance of the battery under the hydrogen sulfide environment. As shown in Fig. 11. The hydrogen sulfide that is added to the anode will undergo chemical reaction (1) and (2) where the oxygen ions are transported by the electrolyte from cathode. For the anode materials itself, the formation of SrS or FeS under the reaction conditions predicted by the thermodynamic calculations will adhere to the active site and influence the porosity causing a decline in the battery performance. SO_2 , H_2S and H_2O will

also adsorb on the catalyst surface. However, under the influence of oxygen ions, SO_2 , H_2S and H_2O will continue to be oxidized to sulfate. This result is consistent with the XPS results, where no peaks for SrS and FeS were observed. The XPS results also confirmed that FeSO_4 is generated, but no SrSO_4 was generated. Therefore, to a certain extent, the formation of FeSO_4 may have hindered the generation of SrSO_4 , therefore, iron doping resulted in the metal sulfate inhibiting the sulfonation of strontium. The results from similar studies have reported enhancement in the sulfur tolerance of $\text{La}_{0.7}\text{Sr}_{0.3}\text{CoO}_3$ perovskite by the addition of iron, which inhibited the sulfonation of strontium [45]. Under the reaction conditions, $\text{Fe}_2(\text{SO}_4)_3$ can be excluded, due to its direct decomposition into iron oxide and sulfur trioxide at 480°C . Sr^{2+} play a decisive role in maintaining oxygen vacancies in YSCF. The oxygen vacancies are closely related to maintaining the electrochemical performance and catalytic properties. Although the existence of FeSO_4 is a hybrid phase for YSCF, its content is very low, which made it difficult to directly observe via XRD. The content of FeSO_4 was determined by XPS. However, the effect on the electrochemical performance and stability are still not clear. Based on the analysis of the electrochemical performance and XPS results, the emergence of FeSO_4 in the sulfur treatment would play an important role to in-preventing sulfur-poisoning. Its influence will occupy a certain amount of TPB, resulting in an increase in the polarization impedance affecting the performance of the SOFC [46]. However, its existence inhibits the generation of strontium sulfate, which results in the anode retaining its fine porous microstructure after the cell tests. A subtle change in the surface morphology was observed between the fresh and reduced cells.

4. Conclusions

YSCF has shown promising results as a SOFC operating with H_2S and sulfur-containing fuels. For the cell containing YSCF-SDC/SDC/Ag, the maximum open circuit voltage was 0.96 V and the maximum power density was 86.34 mW cm^{-2} in $10\%\text{ H}_2 + 1000\text{ ppm H}_2\text{S-N}_2$ at 600°C . The area specific resistance significantly decreases as the temperature increases. The polarization resistance is the primary source affecting the performance of the cell at low temperatures. At a modest firing temperature of 1000°C , the solid-state reaction didn't occur between YSCF and SDC, which would not have a detrimental effect on the oxygen reduction process. A small substitution Sr^{2+} for Y^{3+} in YCrO_3 resulted in the formation of an oxygen vacancy-disordered perovskite oxide. Iron ions in the oxide were primarily in the $2+$ and $3+$ oxidation states. Although the emergence of FeSO_4 was observed after the sulfur treatment, as determined by XPS, the anode retains its fine porous microstructure after the cell tests.

Acknowledgments

This work was financially supported by the National Natural Science Foundation of China (Grant No. 21207064). We would like to specifically thank: Dr. Wang Wei, Dr. Shi Huan-Gang, Dr. Zhang Zhen-Bao and Dr. Gao Xiao-Jia for their interest and comments on this work.

References

- [1] Z. Shao, W. Zhou, Z. Zhu, *Prog. Mater. Sci.* 57 (2012) 804–874.
- [2] J.R. Selmán, *Science* 326 (2009) 52–53.
- [3] N.U. Pujare, *J. Electrochem. Soc.* 134 (1987) 2639.
- [4] H. Kurokawa, L. Yang, C.P. Jacobson, L.C. De Jonghe, S.J. Visco, *J. Power Sources* 164 (2007) 510–518.
- [5] T.S. Li, W.G. Wang, *J. Power Sources* 196 (2011) 2066–2069.
- [6] B.C. Steele, A. Heinzel, *Nature* 414 (2001) 345–352.
- [7] Y.H. Huang, R.I. Dass, Z.L. Xing, J.B. Goodenough, *Science* 12 (2006) 254–257.
- [8] T. Suzuki, Z. Hasan, Y. Funahashi, T. Yamaguchi, Y. Fujishiro, M. Awano, *Science* 325 (2009) 852–855.
- [9] N. Danilovic, J.L. Luo, K.T. Chuang, A.R. Sanger, *J. Power Sources* 192 (2009) 247–257.
- [10] M.Y. Gong, X.B. Liu, J. Tremblay, C. Johnson, *J. Power Sources* 168 (2007) 289–298.
- [11] D. Xu, Y. Bu, W. Tan, Q. Zhong, *Appl. Surf. Sci.* 268 (2013) 246–251.
- [12] M. Ardit, G. Cruciani, M. Dondi, M. Merlini, P. Bouvier, *Phys. Rev. B* 82 (2010).
- [13] T.R. Armstrong, J.W. Stevenson, D.E. McCready, S.W. Paulik, P.E. Raney, *Solid State Ionics* 92 (1996) 213–223.
- [14] W.J. Weber, C.W. Griffin, J.L. Bates, *J. Am. Ceram. Soc.* 70 (1987) 265–270.
- [15] S.L. Wang, B. Lin, Y.C. Dong, D.R. Fang, H.P. Ding, X.Q. Liu, G.Y. Meng, *J. Power Sources* 188 (2009) 483–488.
- [16] M. Ardit, M. Dondi, G. Cruciani, F. Matteucci, *Mater. Res. Bull.* 44 (2009) 666–673.
- [17] T. Tachiwaki, Y. Kunifusa, M. Yoshinaka, K. Hirota, O. Yamaguchi, *Mat. Sci. Eng. B: Solid* 86 (2001) 255–259.
- [18] M.R. Kosinski, R.T. Baker, *J. Power Sources* 196 (2011) 2498–2512.
- [19] W.-C. Wu, J.-T. Huang, A. Chiba, *J. Power Sources* 195 (2010) 5868–5874.
- [20] P. Lohsoontorn, D.J.L. Brett, N.P. Brandon, *J. Power Sources* 175 (2008) 60–67.
- [21] Y. Lin, C. Su, C. Huang, J.S. Kim, C. Kwak, Z. Shao, *J. Power Sources* 197 (2012) 57–64.
- [22] H.S. Song, W.H. Kim, S.H. Hyun, J. Moon, J. Kim, H.-W. Lee, *J. Power Sources* 167 (2007) 258–264.
- [23] C.N. Munnings, S.J. Skinner, G. Amow, P.S. Whitfield, I.J. Davidson, *Solid State Ionics* 177 (2006) 1849–1853.
- [24] J. Zhang, Y. Ji, H. Gao, T. He, J. Liu, *J. Alloys Compd.* 395 (2005) 322–325.
- [25] C. Jin, J. Liu, W. Guo, Y. Zhang, *J. Power Sources* 183 (2008) 506–511.
- [26] C. Fu, K. Sun, N. Zhang, X. Chen, D. Zhou, *Electrochim. Acta* 52 (2007) 4589–4594.
- [27] T. Tachiwaki, Y. Kunifusa, M. Yoshinaka, K. Hirota, O. Yamaguchi, *Int. J. Inorg. Mater.* 3 (2001) 107–111.
- [28] L. Aguilar, S. Zha, Z. Cheng, J. Winnick, M. Liu, *J. Power Sources* 135 (2004) 17–24.
- [29] K. Sundmacher, *Ind. Eng. Chem. Res.* 49 (2010) 10159–10182.
- [30] K.J. Yoon, C.A. Coyle, O.A. Marina, *Electrochem. Commun.* 13 (2011) 1400–1403.
- [31] Z. Cheng, S.W. Zha, M.L. Liu, *J. Electrochem. Soc.* 153 (2006) A1302–A1309.
- [32] Z. Cheng, S.W. Zha, M.L. Liu, *J. Power Sources* 172 (2007) 688–693.
- [33] N. Danilovic, J.L. Luo, K.T. Chuang, A.R. Sanger, *J. Power Sources* 194 (2009) 252–262.
- [34] C.M. Grgicak, R.G. Green, J.B. Giorgi, *J. Power Sources* 179 (2008) 317–328.
- [35] J.-D. Kim, G.-D. Kim, J.-W. Moon, Y.-i. Park, W.-H. Lee, K. Kobayashi, M. Nagai, C.-E. Kim, *Solid State Ionics* 143 (2001) 379–389.
- [36] H. Zhang, X. Ma, J. Dai, S. Hui, J. Roth, T.D. Xiao, D.E. Reisner, *Solid State Ionics* 756 (2003) 491–496.
- [37] K. Kammer, *Solid State Ionics* 177 (2006) 1047–1051.
- [38] P.K. Cheekatamarla, A.M. Lane, *J. Power Sources* 152 (2005) 256–263.
- [39] S.M. Bukhari, J.B. Giorgi, *Solid State Ionics* 194 (2011) 33–40.
- [40] J.T.S. Tao, S.M. Irvine, J. Plint, *Phys. Chem. B* 110 (2006) 21771–21776.
- [41] T. Herranz, S. Rojas, M. Ojeda, F.J. Pérez-Alonso, P. Terreros, K. Pirotta, J.L.G. Fierro, *Chem. Mater.* 18 (2006) 2364–2375.
- [42] Y. Bu, Q. Zhong, D. Xu, W. Tan, *J. Alloys Compd.* 578 (2013) 60–66.
- [43] K. Jiráková, J. Mikulová, J. Klempa, T. Grygar, Z. Bastl, F. Kovanda, *Appl. Catal. A: Gen.* 361 (2009) 106–116.
- [44] K. Sutthiumporn, T. Maneerung, Y. Kathiraser, S. Kawi, *Int. J. Hydrogen Energy* 37 (2012) 11195–11207.
- [45] A.J. Ma, S.Z. Wang, C. Liu, H. Xian, Q. Ding, L. Guo, M. Meng, Y.S. Tan, N. Tsubaki, J. Zhang, L.R. Zheng, X.G. Li, *Appl. Catal. B: Environ.* 146 (2014) 24–34.
- [46] A.S. Martinez, J. Brouwer, *Electrochim. Acta* 53 (2008) 3597–3609.